photonics

MDPI

Article

Laser Wakefield Photoneutron Generation with Few-Cycle High-Repetition-Rate Laser Systems

Daniel Papp [1], Ales Necas [2,*], Nasr Hafz [1,3], Toshiki Tajima [2], Sydney Gales [4], Gerard Mourou [5], Gabor Szabo [1,6] and Christos Kamperidis [1]

1 ELI-ALPS, ELI-HU Non-Profit Ltd., H-6728 Szeged, Hungary
2 TAE Technologies, 19631 Pauling, Foothill Ranch, CA 92610, USA
3 Doctoral School of Physics, Faculty of Science and Informatics, University of Szeged, 9 Dóm tér, H-6720 Szeged, Hungary
4 IJCLab, IN2P3/CNRS, University Paris-Saclay, 91405 Orsay, France
5 Ecole Polytechnique, Route de Saclay, 91128 Palaiseau, France
6 Department of Optics and Quantum Electronics, University of Szeged, H-6720 Szeged, Hungary
* Correspondence: anecas@tae.com

Abstract: Simulations of photoneutron generation are presented for the anticipated experimental campaign at ELI-ALPS using the under-commissioning e-SYLOS beamline. Photoneutron generation is a three-step process starting with the creation of a relativistic electron beam which is converted to gamma radiation, which in turn generates neutrons via the (γ, n) interaction in high-Z material. Electrons are accelerated to relativistic energies using the laser wakefield acceleration (LWFA) mechanism. The LWFA process is simulated with a three-dimensional particle in cell code to generate an electron bunch of 100s pC charge from a 100 mJ, 9 fs laser interaction with a helium gas jet target. The resultant electron spectrum is transported through a lead sphere with the Monte Carlo N-Particle (MCNP) code to convert electrons to gammas and gammas to neutrons in a single simulation. A neutron yield of 3×10^7 per shot over 4π is achieved, with a corresponding neutron yield per kW of 6×10^{11} n/s/kW. The paper concludes with a discussion on the attractiveness of LWFA-driven photoneutron generation on high impact, and societal applications.

Keywords: laser wakefield acceleration; electron; photoneutron; high-repetition laser; few-cycle laser

Citation: Papp, D.; Necas, A.; Hafz, N.; Tajima, T.; Gales, S.; Mourou, G.; Szabo, G.; Kamperidis, C. Laser Wakefield Photoneutron Generation with Few-Cycle High-Repetition-Rate Laser Systems. *Photonics* **2022**, *9*, 826. https://doi.org/10.3390/photonics9110826

Received: 16 May 2022
Accepted: 22 October 2022
Published: 3 November 2022

1. Introduction

Neutron sources are used in a wide array of applications, ranging from transmutation and incineration of spent nuclear fuel [1,2], neutron imaging [3], radioisotope production for medicine [4], cancer treatment [5], oil-well logging [6], gem colorization [7], driving subcritical nuclear fission reactors [8], security applications [9] and many others.

Neutron sources can be divided into three broad categories depending on their size: small, medium and large. A small size source generates a neutron intensity less than $\mathbf{10^9}$ n/s and is based on a natural decay of a radioisotopes. Few prominent examples are the AmBe source based on natural alpha emitters (Am) which induce (alpha, n) reactions on the Be9 target to generate neutrons; another source is Cf-252 based on a spontaneous fission. Medium-sized sources generate neutron intensity in the range of $\mathbf{10^9}$–$\mathbf{10^{13}}$ n/s. They are based on hadron and electron accelerators. In case of hadrons, either a low energy proton or deuteron irradiate a low-Z target such as beryllium or lithium to generate neutrons via stripping or a knock-out process; in contrast, a relativistic proton beam irradiates a high-Z target, e.g., lead, to initiate the spallation process. In case of electrons, a relativistic electron beam impinges on a high-Z material, e.g., lead, tungsten, etc., to convert to gammas via the bremsstrahlung process; generated gamma interacts with an atomic nucleus via the giant dipole resonance mechanism to eject neutrons. Large-size neutron sources are capable

for producing large intensity, far exceeding $\mathbf{10^{16}}$ n/s, and are associated with nuclear fission reactors.

One method of generating high-current (beyond 10^{12} n/s) neutron sources is using an RF LINAC electron accelerator, where the electron beam is absorbed in a high-Z target, and the generated bremsstrahlung interacts with the same target, generating photoneutrons. Experimental demonstrations and characterizations have been carried out earlier at the nELBE facility [10], utilizing a 1 mA 40 MeV electron beam. In an alternative configuration, electrons are converted to gamma in a first-stage converter and transported to a neutron generator. This configuration has been employed in the PARRNe experiment [11,12] with a W-converter and uranium carbide (UC_x) neutron generator that can produce $\mathbf{10^{13}}$ fissions/s using a 100 kW beam of 30 MeV electrons as part of the ALTO project. Another facility [13] is already under implementation, using a 100 MeV, 100 kW electron beam driver, with a maximum-predicted neutron current of 1–4 $\times$ 10^{14} n/s. The high-Z target can be liquid lead [10], tungsten, or even enriched uranium [14,15]. High-intensity electron beams with currents exceeding 10 A can generate a peak neutron yield of $\mathbf{10^{10}}$ n/pulse, as demonstrated at the GELINA facility [16], and $\mathbf{10^{12}}$ neutron/pulse at ORELA [17], with both facilities able to achieve a repetition rate of 100 Hz. An overview of the present and upcoming neutron generator facilities leveraging particle beams was presented in [18].

Advances in laser technology also led to the demonstration of laser-driven photoneutron sources by several groups. One scheme generates electrons using the interaction of a strongly focused laser pulse on a solid (or close to solid) density target [19–21]. However, these sources, utilizing solid targets, are suffering from the limited, low-repetition rate on the solid-state targetry design [22].

Another laser-based neutron generation method relies on electron acceleration via laser wakefield acceleration (LWFA) in plasma [23]. Here, a short-laser pulse is focused on a gas target (gas jet or gas cell); this generates relativistic electrons in an acceleration length of a few mm, then is directed into a high-Z converter. In this scheme, the RF accelerators are essential and are replaced with a laser-driven plasma accelerator, potentially allowing a compact, tabletop-size experimental setup. The laser target itself is a gas jet or gas cell, which allows for operations at repetition rates of 1 kHz [24,25]. The viability of this method has already been demonstrated in the single-shot mode [26], where a tungsten converter was inserted in a 37 MeV-average-energy electron beam, generating few MeV neutrons.

In this paper, we investigate photoneutron generation using a laser wakefield acceleration (LWFA) electron source driven by a high-repetition-rate laser. Simulations have shown that 100 MeV of electron energy can be efficiently reached by relatively modest laser parameters (100 mJ pulse energy) [27], and ultrashort-pulse lasers with a similar pulse energy are available working at a 1 kHz repetition rate [28]. The laser plasma interaction generating and accelerating the electrons is simulated using a multidimensional (3d3v) particle-in-cell (PIC) code, EPOCH [29]. The subsequent electron interaction with matter—including gamma generation and neutron production—is simulated using the Monte Carlo N-Particle (MCNP) code [30].

The paper is organized in the following structure: Section 2 describes the principles of laser wakefield acceleration and presents the simulation results, including the electron energy spectrum. In Section 3, the electron spectrum is used to generate photons and photoneutrons. Additionally, in Section 3, a detailed study of photoneutron generation by a monoenergetic electron beam is given. In Section 4, we will discuss applications and the utilization of the generated neutrons, and we will concentrate on the transmutation of the spent nuclear fuel; radioisotope production, namely, the molybdenum-99 as a precursor to Tc-99; and neutron imaging.

2. Laser Electron Acceleration

The principle of LWFA is to send a short laser pulse through an under-dense gas (usually He, or N), where the laser leading edge also ionizes the gas, turning it into plasma. The mechanism that follows utilizes the laser's radiation pressure (ponderomotive force) to

push aside plasma. At sufficiently high laser intensities, the electrons are removed from the axis of propagation of the laser, and a nonlinear plasma wake forms with close-to-spherical "bubbles" that contain no electrons inside [31–33], with a characteristic size of the plasma wavelength $\lambda_p = 2\pi c/\omega_p$—this is the so-called bubble or blow-out regime where $\omega_p = \sqrt{n_0 e^2/\, m_e \epsilon_0}$ is the plasma frequency and n_0 is the plasma electron density. This regime requires that the laser pulse length $c\tau_L$ is not larger than the plasma bubble. Note that the plasma wavelength decreases with density as $\sim n_0^{-1/2}$, so a shorter laser pulse length is required to permit the blow-out regime at higher densities.

This laser wake travels with the group velocity of the laser in the plasma (which equals the group velocity of light) $v_p = v_g = c\sqrt{1 - \omega_p^2/\omega_L^2}$. In this ion cavity, the charge distribution produces a longitudinal electric field. Here, τ_L is the laser pulse duration and ω_L is the laser frequency. The diameter of the laser focal spot must also be of similar magnitude, in the order of 10 μm.

The acceleration process is also helped by relativistic plasma self-focusing [34], which keeps the laser focus from diverging, helping it to propagate further in the plasma, preserving its high intensity, and the conditions necessary for the blow-out regime.

If electrons are injected at the back end of the bubble, they will be accelerated until they reach the mid-point of the plasma bubble, where the acceleration field is zero. As the bubble itself moves close to the speed of light, the electrons are eventually accelerated to relativistic velocities. Depending on the density of the plasma, the electron acceleration is generally limited by dephasing (the electrons reach the midpoint of the bubble) or the depletion of the laser pulse, with the latter being dominant at shorter laser-pulse lengths [33].

In this paper, we analyze photoneutron generation, assuming a state-of-the-art laser system, similar to the one described in [28], with the assumed parameters of 100 mJ (nominal) pulse energy, 8 fs FWHM pulse duration, 6 μm FWHM focal spot, and 900 nm central wavelength. The energy content of the laser electric field in the simulation was 112 mJ. These figures correspond to the expected laser parameters of the SYLOS3 laser (currently under development) at ELI-ALPS.

The simulation of the laser wakefield acceleration follows the same approach as described in Papp et al. [27]. Simulations have been carried out using the EPOCH3D [29] particle in the cell code. A moving window reference frame was applied, moving with the phase velocity of the laser pulse. The dimensions of the simulation domain are $x \times y \times z = 24 \times 24 \times 24$ μm and are subdivided by $480 \times 120 \times 120$ cells with 4 macroparticles per cell, applying a fourth-order electromagnetic solver which limits the numerical dispersion effects.

The longitudinal plasma profile had half(semi)-gaussian entrance and exit ramps of 100 μm length (between 10% and 90% density values), with a flat density in between, at 400 μm length (between 90% densities of the entrance and exit ramps). This plasma length was optimized, and was longer than the nominal depletion length of 218 μm. The electron density in the flat region was 1.5×10^{19} cm^{-3}, which is optimal based on preliminary simulations. The plasma was a pure He gas.

The electron density can be seen in Figure 1a. The electron distribution function and spectrum is shown in Figure 1b,c, respectively. The spectrum is broad, with a well-defined quasi-monoenergetic peak at 110 MeV. The spectrum also has an exponential tail past 180 MeV—the high-space charge causes the electron bunch to expand, and it accelerates the front end of the bunch further. The average energy of the electron bunch is 70 MeV with a bunch charge of 453 pC (3×10^9 electrons). While the broadband nature of the electron spectrum might not be suitable for some applications, in the generation of photoneutrons, the spectral quality of the beam is of secondary importance.

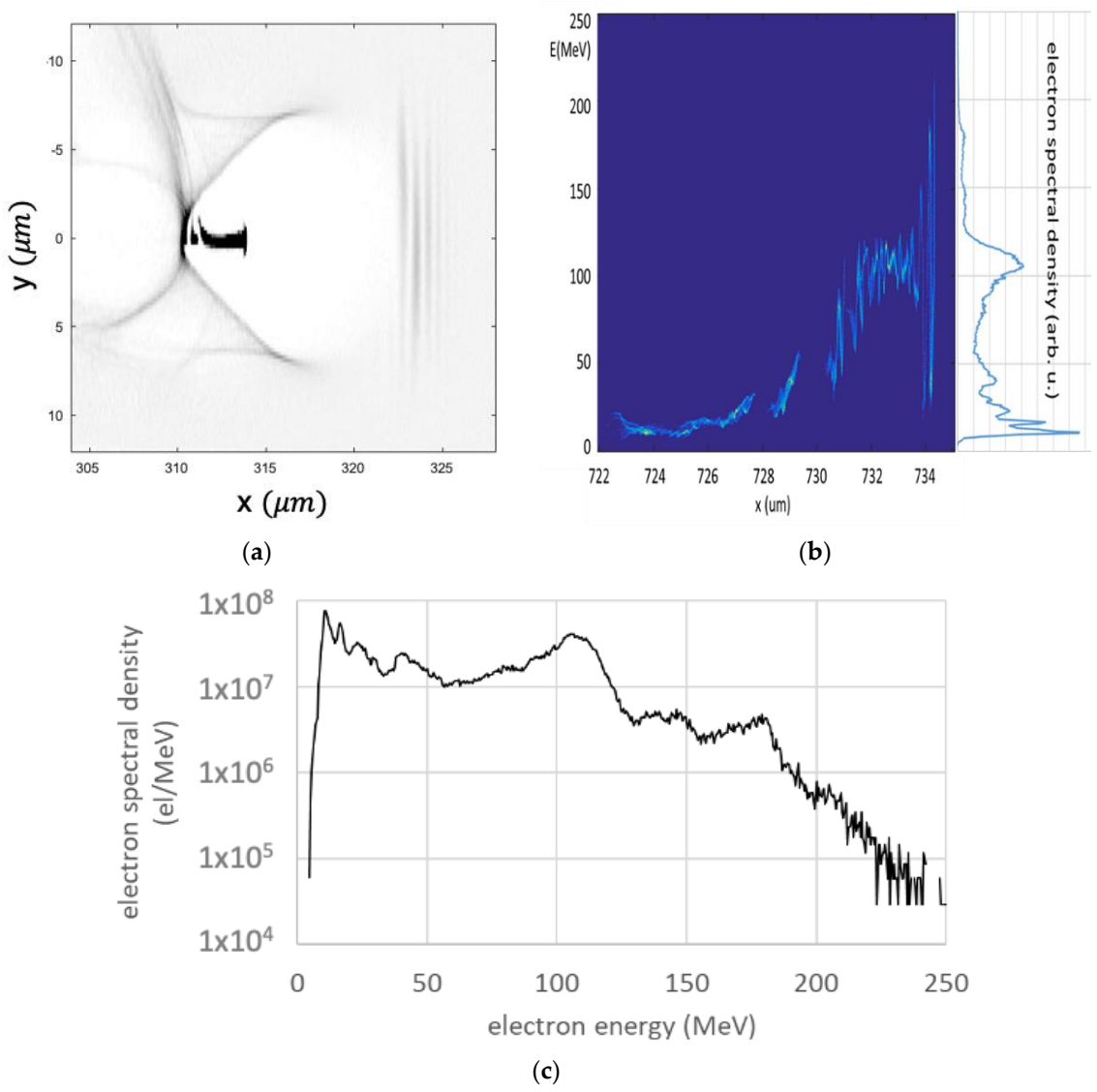

Figure 1. Electron density at the center of the density plateau (**a**), electron distribution function and spectrum after the plasma (**b**), spectrum on a log-lin plot (**c**).

The efficiency of the electron acceleration at these laser pulse parameters is very high; the accelerated electron bunch has a total energy of 32 mJ, which corresponds to a 29% laser-to-electron conversion efficiency. The cause of this high conversion efficiency is the strong coupling between the laser and the plasma and the high bunch charge (number of accelerated electrons). As discussed above, the short laser pulse duration allows for higher plasma densities. The higher plasma density permits the self-focusing of the laser for the whole length of the plasma accelerator, keeping the laser pulse intensity sufficiently high for the blow-out regime. The short pulse duration also shortens the depletion length [33], allowing for the transfer of the majority of the laser energy into the plasma. After 500 µm of propagation, at the end of the plasma plateau, 61% of the laser energy is spent, mostly exciting the plasma wake (some of it also diffracted out of the domain). The energy into the plasma wake then goes into accelerating the electron bunch. The high density provides a sufficient number of electrons to be accelerated. It must be noted that conversion efficiencies of 3% are demonstrated in LWFA experiments with TW-class lasers [25], and with higher laser energies, conversion efficiencies above 10% are expected [35].

3. Photoneutron Generation

Photons usually interact with atomic electrons or with the nuclear field, leaving the nucleus unaffected; however, a sufficiently large energy gamma photon may overcome the neutron binding energy to cause a (γ, n) reaction to eject a neutron from the nucleus as a result of the giant dipole resonance (GDR) mechanism. Photon energy is transferred to the nucleus by the oscillating electric field of the photon, which induces oscillation among the nucleons. Photoneutron production is more probable than proton ejection, since the latter requires the need to overcome the Coulomb barrier.

Intense photoneutron production can thus be realized via a bremsstrahlung converter, with the neutron energy spectra extending to 10 MeV and peaking around 1 MeV. The process is initiated via an energetic-electron bombard high-Z material (e.g., lead, tungsten or uranium) to generate energetic gamma rays with an energy spectrum extending up to the most energetic electron. The cross-section of the (γ, n) reaction increases with photon energy, reaching a maximum over a broad energy range of approximately 12 to 16 MeV for medium and heavy nuclei. The peak energy of the GDR can be approximated [36] by 80 $A^{-1/3}$ MeV for A > 40, where A is the atomic mass number, e.g., 208 for lead, which corresponds to 13.5 MeV. The width of the resonance is 3 MeV for lead, as shown in Figure 2. The neutron binding energy for Pb-208 is 7.8 MeV, indicating a threshold energy for the photon. This fact is also reflected in Figure 2 as the threshold energy.

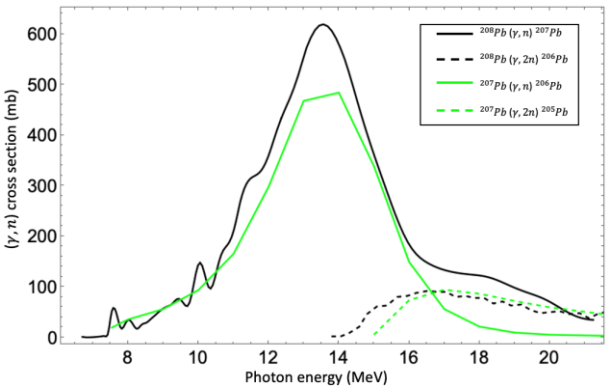

Figure 2. Photonuclear cross-section for two isotopes of lead, obtained from the END-F and TENDL cross-sectional libraries.

Above the photon energy of 35 MeV, the photoneutron production is mainly due to the quasi-deuteron (QD) effects. In this process, the photon interacts with the dipole moment of the proton–neutron pair rather than the nucleus as a whole.

The electron–matter interaction is collision-dominated for electron energy lower than 10 MeV and a radiative interaction process that dominates high-energy electrons. The collisional interaction is described by the Bloch–Bethe formulae proportional to Z (atomic number), whereas the radiation process is described by the bremsstrahlung process proportional to Z^2. Thus, to increase the electron–matter interaction, energetic electrons and a choice of high-Z converter material are needed. For the study presented in this paper, we select the naturally occurring lead. Although complex geometries are readily modelled using the MCNP code, we have chosen the simple geometry of a lead sphere with a density of ρ = 11.35 g/cm^3, and an isotropic electron source at its origin. The MCNP code samples from the electron distribution and utilizes END-F cross-sections and models to convert them to photons, and subsequently, from photons to neutrons. Thus, a comprehensive electron, photon and neutron transport is realized. A total of 10^8 histories are run to maintain an error below 3% for all the energy bins. Furthermore, since the (γ, n) reaction has a threshold of 7 MeV, we remove all electrons and photons with energy less than 5 MeV from the simulation which speeds up computation, but as a consequence, suppresses all positron annihilation processes.

The pertinent metric for the photoneutron generation is the yield of neutrons generated per electron. We investigated the yield of a mono-energetic electron source located at the center of a natural lead sphere by varying the sphere radius and electron energy. The results are presented in Figure 3 for various electron energies. The LWFA-accelerated electron energy gain is given by the expression $W_e = \frac{2}{3} a_0 m_e c^2 n_c / n_e$, with $a_0 = 3 - 5$, $m_e c^2 = 0.511$ MeV, $n_c / n_e = 100$. Thus, electron energy of 100 MeV is readily achieved. The radiative stopping power in lead for a 100 MeV electron is 150 MeV/cm and the mass attenuation coefficient for 1–100 MeV photon in lead is 0.1 cm^2/g or 1 cm, thus, a lead sphere of 6–8 cm is needed to sufficiently covert electrons to photons and photons to neutrons. For a 100 MeV electron beam, the neutron yield saturates for a sphere radius of 6 cm at around 0.03 n/e, with a yield efficiency of 3×10^{-4} n/e/MeV. In contrast the DT fusion yield is 1×10^{-5} n/d. The yield improves for spallation to 30 n/p; however, a proton with energy over 1 GeV is needed.

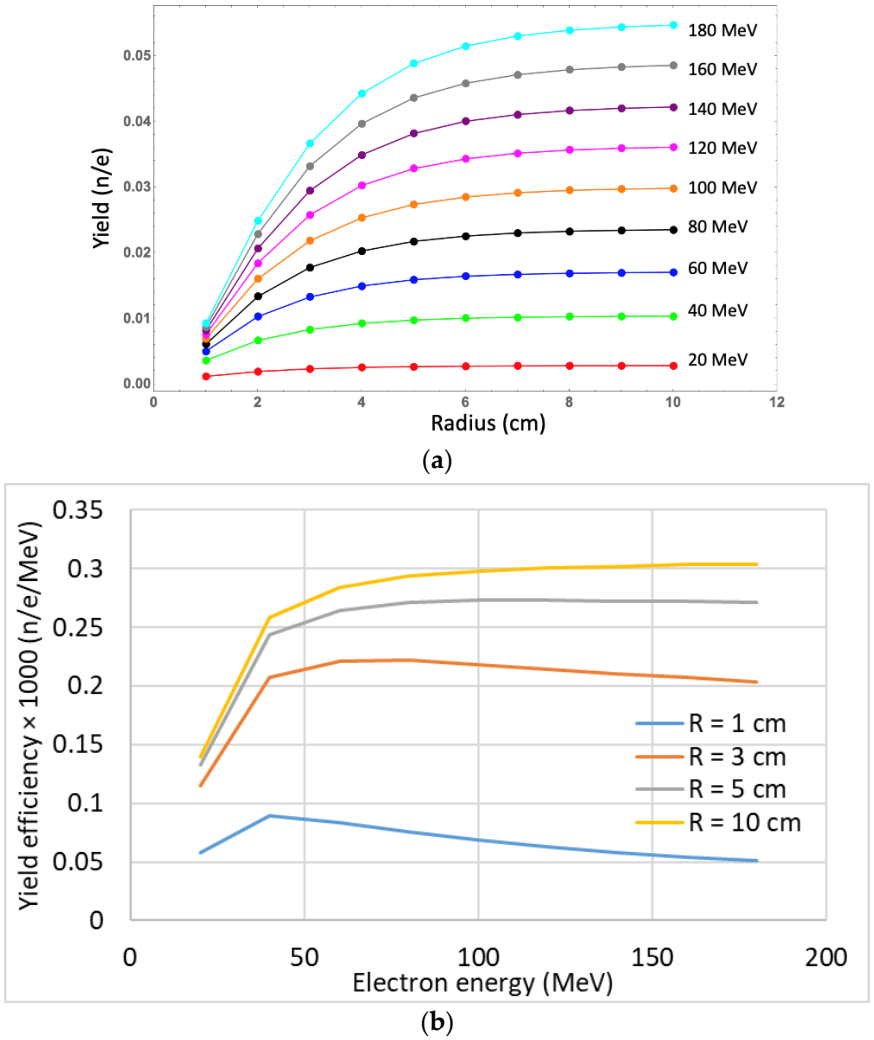

Figure 3. Neutron yield per electron for various electron energies and radius of a lead sphere (**a**), with electrons that are sourced at the sphere origin. The efficiency of neutron generation as a function of electron energy (**b**), for selected lead sphere radii.

Figure 3b also shows the energy dependence of the conversion efficiency. Even for larger spheres, the conversion efficiency does not increase significantly beyond 100 MeV. As a consequence, the requirements on the electron beam quality are relaxed—the electron spectrum should have a significant component above 50 MeV. Since the LWFA electron energy spectrum is complex, it is instructive to study the photoneutron generation using

monoenergetic electrons. In this example, 20 MeV and 50 MeV isotropic electron sources are introduced at the center of a 10 cm natural lead sphere. The generated photon energy spectrum is shown in Figure 4, which extends to the highest energy electron. For the 20 MeV case, the average photon energy is 2.8 MeV and yield of 5 photons per electrons. In contrast, the 50 MeV case generates an average photon energy of 4.9 MeV, with a yield of 15 photons per electron. The neutron energy spectra are shown in Figure 5 with a yield of 0.0028 n/e and 0.014 n/e for 20 MeV and 50 MeV electron sources, respectively.

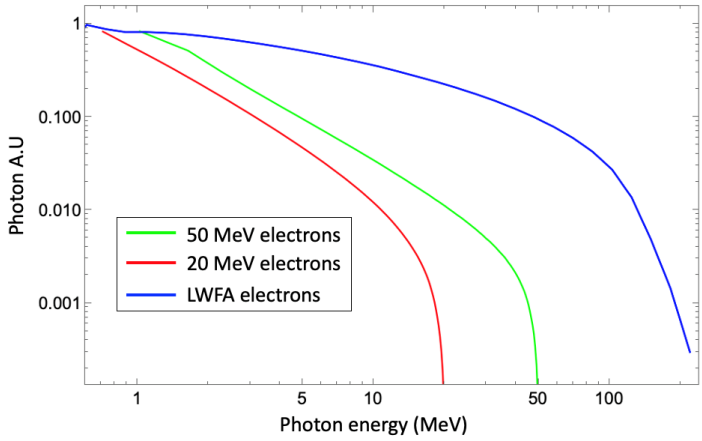

Figure 4. Photon energy spectrum resulting from injecting mono-energetic 20 MeV (red), 50 MeV (green) electrons and LWFA electrons (blue) at a center of a 10 cm lead sphere.

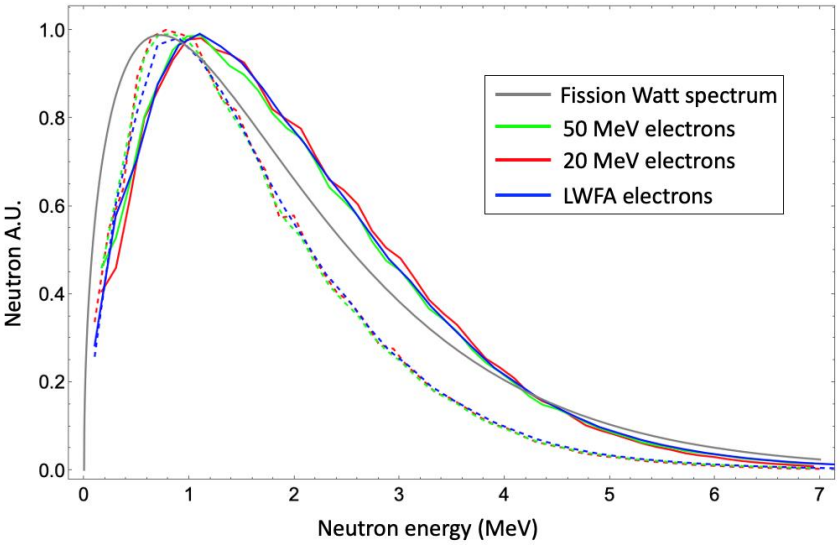

Figure 5. Neutron energy spectra for 20 MeV (red), 50 MeV (green) electron beams and LWFA electrons (blue) sampled at r = 0.5 cm (solid), r = 10 cm (dashed) and Watt fission spectrum (gray) for U-235.

The conversion of electrons to photoneutrons is now studied, utilizing the electron spectrum, as shown in Figure 1. For this study, we increased the number of electrons to transport to 10^9 to have a sufficient sampling of the high-energy electron tail. The highest energy electron bin is 250 MeV, and Figure 4 confirms that the highest energy photon is also 250 MeV. The neutron spectrum from the LWFA electrons is shown in Figure 5.

The summary of results of photoneutron generation from the monoenergetic and LWFA electrons are presented in Table 1. The LWFA electrons' average energy $\langle E_e \rangle$ = 71 MeV. The average photon energy for the monoenergetic cases, 2.6 MeV and 4.9 MeV, respectively, is

not only below the peak of the (γ, n) reaction cross-section, but also below the photoneutron generation threshold energy of 7 MeV. For the electron of the 20 MeV case, 4% of photons contribute to photoneutron generation, this increases to 17% for the electron source of 50 MeV case and 28% for the LWFA electrons. The neutron spectra are shown in Figure 5 along with Watt fission spectrum for comparison. The average neutron energy is same for all cases; however, a moderation is observed when sampling neutrons at r = 0.5 cm and r = 5 cm; i.e., the average energy decreases from 2.0 MeV to 1.7 MeV for all cases. The electron yield, Y_e, can be obtained from the electron creation table in the MCNP output. Besides the original electrons, electrons are generated via pair production, Compton recoil, photo-electric and knock-on effects; for this analysis, we lowered the cut-off energy to 0.5 MeV. In contrast, the photons are predominantly generated via bremsstrahlung and positron annihilation with a yield shown in Table 1. Lastly, the neutron yield, Y_n, is shown in the last column.

Table 1. Yields and average energies for the monoenergetic and LWFA electron sources.

Energy (MeV)	$\langle E_\gamma \rangle$ (MeV)	$<E_n>$ (MeV)		Y_e	Y_y	Y_n
		0.5 cm	5 cm			
20	2.6	2.0	1.7	6.3	5	0.003
50	4.9	2.0	1.7	16	15	0.01
LWFA ($<E_e>$ = 71 MeV)	11.3	2.0	1.7	23	23	0.02

In Section 2, we reported 3×10^9 electrons in the bunch at the laser exit, which generates 6×10^7 neutrons using the yield $Y_n = 0.02$ n/e. Since the 100 mJ laser has been used, an efficiency of 6×10^{11} n/s/kW is obtained. This neutron yield is similar to the experimental work of Gu et al. [37], however, with a 120 J laser. The efficiency is in line with electron linac generators [38] and exceeds 140 neutrons per shot reported in [39] for d(d, n)^{3}He fusion reactions using 200 mJ and a 160 fs laser.

4. Photoneutron Applications

In the introduction, we highlighted a wide spectrum of neutron applications of global importance. In this section, we will focus on such applications and we will quantify the attractiveness of our proposed LWFA-driven neutron generation approach:

(a) Medical radio-isotope production (Moly-99 to Tc-99 precursor);
(b) Incineration of spent nuclear fuel;
(c) Neutron radiography/imaging.

4.1. Medical Radioisotope Production

Over 40 million medical imaging procedures are performed with the radioisotope technetium-99m per year. Tc-99m can be generated from the decay of the parent molybdenum-99 nuclei with a half-life of 66 h. Mo-99 is generated in a nuclear reactor as a result of the fission products with a 6.1% yield, as shown in Figure 6.

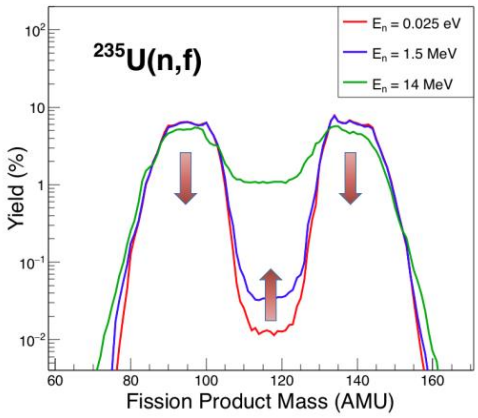

Figure 6. Fission product yield for various neutron energy bombardment. ^{99}Mo yield from fission is 6% of all the fission products. Adapted from data from T.R. England and B.F. Rider, LA-UR-94-3106 (1994).

However, and mainly due to the overall controversy around the future of nuclear power, there is a severe shortage of Tc-99m, and thus, many imaging procedures are postponed or cancelled. An alternative to a nuclear reactor is a sub-critical assembly irradiated by, e.g., DT fusion neutrons, which is a path that Shine Medical [10] is following. Their approach is to utilize a ~100s keV electrostatically accelerated deuteron beam impinging on a tritium target (gas or solid) to produce 14 MeV neutrons, with the neutrons subsequently interacting with 20% of enriched U-235 to produce Mo-99. Shine Medical's approach is constrained by tritium, which by itself imposes certain constraints in production, delivery logistics and handling.

In this report, we propose to generate laser-driven LWFA electrons to produce Mo-99 by photoneutrons, where high-energy electrons interact with high-Z material (as described in the introduction)—e.g., lead, tantalum or uranium, to convert to gamma—via bremsstrahlung, which in turn, interacts with a nucleus through the (γ, n) reaction. However, a direct pathway for irradiating a uranium assembly directly with laser-generated electrons is also an option (photofission).

Average single imaging or treatment with Tc-99m utilizes 30 mCi, assuming 5.2×10^6 Ci/g, which translates to a single treatment requiring 5.4 ng of Tc-99m. A high average-power laser can generate a sufficient amount of Mo-99. (From Section 3, we estimate that we can obtain 6×10^7 n per laser shot, for a Mo-99 yield of 6.1 %. Using these numbers, we can estimate to generate the required Mo-99 amount in 10 s using a 1 MHz laser or 10^4 s for a 1 kHz laser. An improvement factor of 10 could be achieved if we use electron irradiation of an enriched U-235 assembly directly together with a double-stage multiplier, a possibility we intend to explore in our proposed experiment. Considerations of such duty-cycle were not taken into account in this study).

4.2. Transmutation of Spent Nuclear Fuel

Conventional nuclear power plants, whether run in a critical or a sub-critical operation, will generate spent nuclear fuel (SNF) as a waste product. The waste can be split into two main components:

(1) Fission products such as iodine, strontium, molybdenum, etc.
(2) Actinides such as plutonium and isotopes of uranium and thorium and minor actinides (americium, curium and neptunium).

The management of SNF is usually carried out by partitioning and transmutation (P&T), whereas uranium and plutonium (partially) are removed by the PUREX process, and the P&T proceeds with sending the MA and long-lived fission products to transmuta-

tion. Transmutation is accomplished by irradiation of the partitioned SNF with neutrons. One example of transmutation by fission is shown here:

$$n + {}^{240}Pu \text{ (24,000 years)} \rightarrow {}^{134}Cs \text{ (2 years)} + {}^{104}Ru \text{ (stable)} + 2\,n + energy$$

Pu-240 has a half-life of 24,000 years; however, when bombarded by neutrons, Pu-240 fissions into Cs-134 and Ru-104 plus neutrons and energy. Thus, in this particular example, we have reduced the required storage duration by 10,000-fold. The motivation for the transmutation of nuclear waste is shown in Figure 7 by comparing the overall SNF radiotoxicity to the reference of naturally occurring uranium (green line) necessary to fabricate 1 ton of enriched uranium fuel. The reference is radiotoxicity associated with uranium and its radioactive progenies. The reference radiotoxicity is reached after a period of 130,000 years for nuclear waste if left untreated, which is also called the open cycle. In contrast, a complete partitioning and transmutation without any losses can shorten the duration to 270 years (brown curve—fission products) and decrease the storage volume by a factor of 10, which is also called a fully-closed cycle. At this point, only fission product's radiotoxicity contributes. The long-term radiotoxicity is mainly dominated by transuranic elements, in particularly the Am-241 and several isotopes of plutonium (Pu-239, Pu-240, Pu-241) and their descendants. However, several long-lived fission products contribute to long-term radiotoxicity with Tc-99, I-129, Cs-135, Zr-93 and Pd-107 as the prominent examples. Iodine and cesium are the most problematic as they readily diffuse out of geological repositories and reach the biosphere.

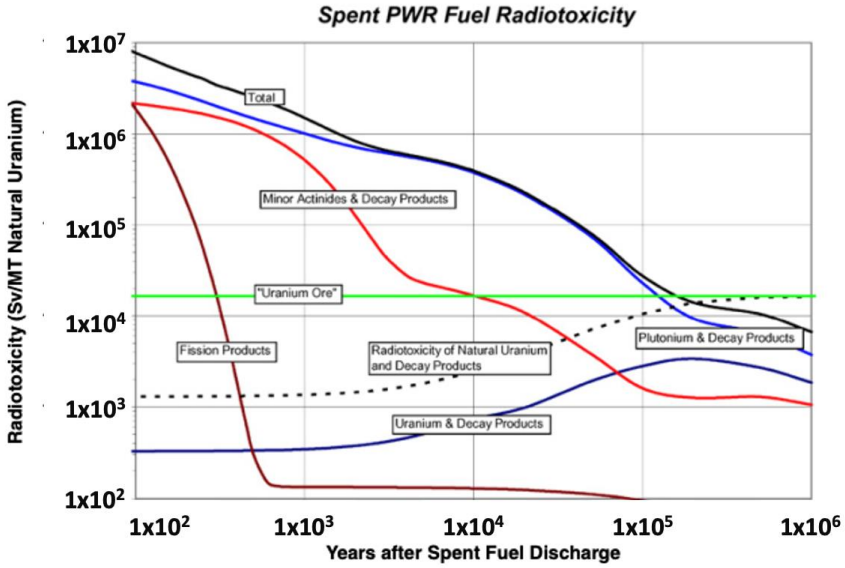

Figure 7. Motivation for transmutation adapted from [40]. Comparison of the radiotoxicity of nuclear waste from uranium-based PWR to that produced by the naturally occurring uranium needed to generate 1 metric ton of enriched uranium. Permission to reuse figure granted from Elsevier.

The transmutation of the MA must be performed in a sub-critical assembly ($k_{eff} < 1$) due to their neutron-rich isotopes, i.e., it is difficult to maintain criticality with a large MA present. Thus, we propose to utilize laser-generated photoneutrons to drive the transmutation of MA and long-lived fission products.

4.3. Neutron Radiography/Imaging and Neutron Spectroscopy

Neutrons, through their high interaction with light elements and a weak interaction with the heavy elements, are ideal to non-destructively penetrate and imagine the content of metal containers, e.g., shipping containers or car spark plugs, as shown in Figure 8. The laser-generated photoneutrons are ideally suited for this application. However, it is

required to collimate and create a quasi-monoenergetic neutron beam that is optimized for various imaging applications. Using neutrons helps to locate rare-earth metals, can analyze whether a canister with fuel is filled, check whether O-rings fit snuggly after assembly (space rocket where further corrections are impractical), etc. Neutron spectroscopy, which utilizes laser-generated neutrons, has been proposed [41,42].

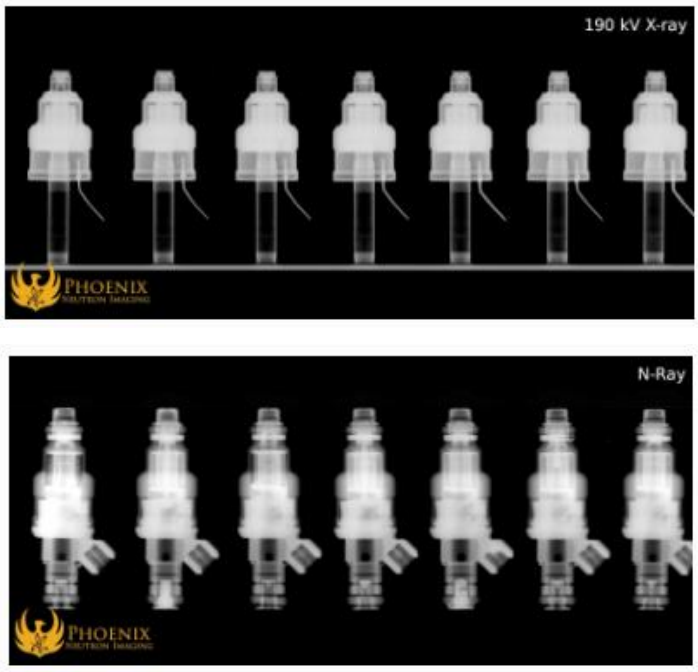

Figure 8. Comparison of imaging using X-rays (**top**) and neutrons (**bottom**). Used with permission.

5. Conclusions

We present computational estimates on photo-neutron generation, using laser-driven LWFA electron sources as the neutron drivers. Due to the rapid progress in high-average power, high-repetition-rate laser technology, such as electron sources, are in a development phase within the laser plasma acceleration community. Specifically, and pertinent to the present work, all calculations have been performed with the eSYLOS electron beamline at ELI-ALPS, Hungary [43], with which we propose to utilize (once commissioned) for the purposes of demonstrating a novel neutron generation scheme, with comparable or better yields to other laser-driven neutron sources. Our goal is to perform proof-of-principle experiments which we later intend to optimize as the neutron source with the abovementioned laser and electron source infrastructure.

The applications targeted are of high societal importance, with the added benefit of being forgiving to the required initial electron beam quality and specifications, something that laser-driven LWFA electron sources can nowadays routinely deliver. With the advent of 1 kHz few TW laser systems, we envision our proposal as the first stepping stone for introducing these laser/LWFA-driven neutron sources to these important societal applications, and as the first necessary step to ramp up to even higher repetition rates (1 MHz range) once the future generation of laser systems manifests.

The photoneutron generation presented is largely unoptimized. As a future work, we propose to optimize the electron density and electron profiles to achieve higher efficiency based on the curves in Figure 3a,b. We can observe that beyond the electron energy of 100 MeV, the yield of n/e/MeV is improved only marginally. Further, we propose to modify the converter with other materials, e.g., tungsten, tantalum, or even fissile material such as low-enriched uranium. An additional conversion of ^{9}Be is proposed to leverage the (n, $2n$) reaction.

Particle accelerators have, approximately, a 100-year history (1924 Gustav Ising) of development, and although they have come a long way since then, they are still bulky and costly machines. The laser driven electron sources must compete with the state-of-the-art industrial electron beam (IBA [44], KIPT [13]) regarding energy and current. A laser-generated electron beam current is scalable with an increasing repetition rate and number of beam lines; however, in contrast to the RF sources, they are neither well-collimated nor mono-energetic. These are disadvantages if the beam is required to be transported, but the proposed application relies on in situ electron generation.

Author Contributions: Conceptualization, D.P., A.N., N.H., T.T., S.G., G.M., G.S. and C.K. Formal analysis, D.P.; Writing—original draft, A.N.; Writing—review & editing, D.P. and S.G. All authors have read and agreed to the published version of the manuscript.

Funding: We are thankful for the support of the Hungarian National Research, Development, and Innovation Office through the Hungarian National Laser-Initiated Transmutation Laboratory (NLTL) (contract # NKFIH-877-2/2020), the Norman Rostoker Fund for the research. National Research, Development and Innovation Office of Hungary, Project No. 2020-1.2.4-TÉT-IPARI-2021-00018.

Institutional Review Board Statement: Not applicable.

Informed Consent Statement: Not applicable.

Data Availability Statement: Not applicable.

Acknowledgments: We are deeply indebted to our colleagues Thierry Massard, Peter Taborek, Sumio Iijima, Konstantin Novoselov, Vladimir Shiltsev, Sahel Hakimi, Scott Nicks, Ernesto Barraza, Yves Brechet, Xueqing Yan, Timur Esirkepov, Sergei Bulanov, Tetsuya Kawachi, the late Norman Rostoker, and the late John Dawson for their collaboration, advice, and inspiration.

Conflicts of Interest: The authors declare no conflict of interest.

Dedication: We would like to dedicate this paper to the pioneers, the late V. Veksler and the late N. Rostoker, of the collective acceleration in plasma, whose works we were inspired by and tried to follow. They may be delighted that we came thus far.

References

1. Rubbia, C.; Rubio, J.; Buono, S.; Carminati, F.; Fiétier, N.; Galvez, J.; Geles, C.; Kadi, Y.; Klapisch, R.; Mandrillon, P.; et al. Conceptual Design of a Fast Neutron Operated High Power Energy Amplifier. In *Proceedings of the CERN/AT/95-44, 1995*; CERN: Geneva, Switzerland, 1995; pp. 187–312.
2. Tajima, T.; Necas, A.; Mourou, G.; Gales, S.; Leroy, M. Spent Nuclear Fuel Incineration by Fusion-Driven Liquid Transmutator Operated in Real Time by Laser. *Fusion Sci. Technol.* **2021**, *77*, 251–265. [CrossRef]
3. Woracek, R.; Santisteban, J.; Fedrigo, A.; Strobl, M. Diffraction in Neutron Imaging—A Review. *Nucl. Instrum. Methods Phys. Res. A* **2018**, *878*, 141–158. [CrossRef]
4. Pudjorahardjo, D.S.; Wahyono, P.I.; Syarip. Compact Neutron Generator as External Neutron Source of Subcritical Assembly for Mo-99 Production (SAMOP). *AIP Conf. Proceed.* **2020**, *2296*, 20115.
5. Moss, R.L. Critical Review, with an Optimistic Outlook, on Boron Neutron Capture Therapy (BNCT). *Appl. Radiat. Isot.* **2014**, *88*, 2–11.
6. Frankle, C.M.; Dale, G.E. Unconventional Neutron Sources for Oil Well Logging. *Nucl. Instrum. Methods Phys. Res. A* **2013**, *723*, 24–29.
7. Krambrock, K.; Ribeiro, L.G.M.; Pinheiro, M.V.B.; Leal, A.S.; de BC Menezes, M.Â.; Spaeth, J.-M. Color Centers in Topaz: Comparison between Neutron and Gamma Irradiation. *Phys. Chem. Min.* **2007**, *34*, 437–444. [CrossRef]
8. Gulik, V.; Tkaczyk, A.H. Cost Optimization of ADS Design: Comparative Study of Externally Driven Heterogeneous and Homogeneous Two-Zone Subcritical Reactor Systems. *Nucl. Eng. Des.* **2014**, *270*, 133–142. [CrossRef]
9. Gozani, T.; Morgado, R.E.; Seher, C.C. Nuclear-Based Techniques for Explosive Detection. *J. Energetic Mater.* **1986**, *4*, 377–414.
10. Beyer, R.; Birgersson, E.; Elekes, Z.; Ferrari, A.; Grosse, E.; Hannaske, R.; Junghans, A.R.; Kögler, T.; Massarczyk, R.; Matić, A.; et al. Characterization of the Neutron Beam at NELBE. *Nucl. Instrum. Methods Phys. Res. A* **2013**, *723*, 151–162.
11. Ibrahim, F.; Obert, J.; Bajeat, O.; Buhour, J.M.; Carminati, D.; Clapier, F.; Donzaud, C.; Ducourtieux, M.; Dufour, J.M.; Essabaa, S.; et al. Photofission for the Production of Radioactive Beams: Experimental Data from an on-Line Measurement. *Eur. Phys. J. A-Hadron. Nucl.* **2002**, *15*, 357–360. [CrossRef]

12. Essabaa, S.; Arianer, J.; Ausset, P.; Bajeat, O.; Baronick, J.P.; Clapier, F.; Coacolo, L.; Donzaud, C.; Ducourtieux, M.; Galès, S.; et al. Photo-Fission for the Production of Radioactive Beams ALTO Project. *Nucl. Instrum. Methods Phys. Res. B* **2003**, *204*, 780–784. [CrossRef]
13. Bezditko, A.P.; Gordienko, A.N.; Gladkikh, P.I.; Gvozd, A.M.; Kapliy, D.A.; Karnaukhov, I.M.; Karnaukhov, I.I.; Lyashchenko, V.N.; Mytsykov, A.O.; Moisieienko, M.P.; et al. 100 MeV/100 KW Accelerator Adjustment for the NSC KIPT Neutron Source Physical Start Up. *Probl. At. Sci. Technol.* **2020**, *129*, 135–142.
14. Bezditko, O.; Karnaukhov, I.; Mytsykov, A.; Zelinsky, A.; Tarasov, D. Status of the NSC KIPT Neutron Source. *Energy* **2017**, *2*, 1013.
15. Zelinsky, A.Y.; Bezditko, O.; Demchenko, P.O.; Karnaukhov, I.; Oleinik, V.; Peev, F.; Ushakov, I.; Vodin, O.; Gohar, Y. NSC KIPT Neutron Source on the Base of Subcritical Assembly Driven with Electron Linear Accelerator. In Proceedings of the IPAC 2013, Shanghai, China, 13–17 May 2013.
16. Flaska, M.; Borella, A.; Lathouwers, D.; Mihailescu, L.C.; Mondelaers, W.; Plompen, A.J.M.; van Dam, H.; van der Hagen, T.H.J.J. Modeling of the GELINA Neutron Target Using Coupled Electron–Photon–Neutron Transport with the MCNP4C3 Code. *Nucl. Instrum. Methods Phys. Res. A* **2004**, *531*, 392–406. [CrossRef]
17. Coceva, C.; Simonini, R.; Olsen, D.K. Calculation of the ORELA Neutron Moderator Spectrum and Resolution Function. *Nucl. Instrum. Methods Phys. Res.* **1983**, *211*, 459–467. [CrossRef]
18. Colonna, N.; Gunsing, F.; Käppeler, F. Neutron Physics with Accelerators. *Prog. Part Nucl. Phys.* **2018**, *101*, 177–203. [CrossRef]
19. Pomerantz, I.; Mccary, E.; Meadows, A.R.; Arefiev, A.; Bernstein, A.C.; Chester, C.; Cortez, J.; Donovan, M.E.; Dyer, G.; Gaul, E.W.; et al. Ultrashort Pulsed Neutron Source. *Phys. Rev. Lett.* **2014**, *113*, 184801. [CrossRef] [PubMed]
20. Kleinschmidt, A.; Aumüller, S.; Bagnoud, V.; Jahn, D.; Schanz, V.A.; Zimmer, M.; Roth, M. Moderation of a Laser-Generated Neutron Beam at PHELIX. *Helmholtz Inst. Jena Annu. Rep.* **2018**, *2017*, 37.
21. Günther, M.M.; Rosmej, O.N.; Tavana, P.; Gyrdymov, M.; Skobliakov, A.; Kantsyrev, A.; Zähter, S.; Borisenko, N.G.; Pukhov, A.; Andreev, N.E. Forward-Looking Insights in Laser-Generated Ultra-Intense γ-Ray and Neutron Sources for Nuclear Application and Science. *Nat. Commun.* **2022**, *13*, 170. [CrossRef]
22. Prencipe, I.; Sgattoni, A.; Dellasega, D.; Fedeli, L.; Cialfi, L.; Choi, I.W.; Kim, I.J.; Janulewicz, K.A.; Kakolee, K.F.; Lee, H.W.; et al. Development of Foam-Based Layered Targets for Laser-Driven Ion Beam Production. *Plasma Phys. Control Fusion* **2016**, *58*, 34019.
23. Tajima, T.; Dawson, J.M. Laser Electron Accelerator. *Phys. Rev. Lett.* **1979**, *43*, 267. [CrossRef]
24. Guénot, D.; Gustas, D.; Vernier, A.; Beaurepaire, B.; Böhle, F.; Bocoum, M.; Lozano, M.; Jullien, A.; Lopez-Martens, R.; Lifschitz, A.; et al. Relativistic Electron Beams Driven by KHz Single-Cycle Light Pulses. *Nat. Photonics* **2017**, *11*, 293–296. [CrossRef]
25. Gustas, D.; Guénot, D.; Vernier, A.; Dutt, S.; Böhle, F.; Lopez-Martens, R.; Lifschitz, A.; Faure, J. High-Charge Relativistic Electron Bunches from a KHz Laser-Plasma Accelerator. *Phys. Rev. Accel. Beams* **2018**, *21*, 13401. [CrossRef]
26. Jiao, X.J.; Shaw, J.M.; Wang, T.; Wang, X.M.; Tsai, H.; Poth, P.; Pomerantz, I.; Labun, L.A.; Toncian, T.; Downer, M.C.; et al. A Tabletop, Ultrashort Pulse Photoneutron Source Driven by Electrons from Laser Wakefield Acceleration. *Matter. Radiat. Extrem.* **2017**, *2*, 296–302. [CrossRef]
27. Papp, D.; Lécz, Z.; Kamperidis, C.; Hafz, N.A.M. Highly Efficient Few-Cycle Laser Wakefield Electron Accelerator. *Plasma Phys. Control Fusion* **2021**, *63*, 65019.
28. Toth, S.; Stanislauskas, T.; Balciunas, I.; Budriunas, R.; Adamonis, J.; Danilevicius, R.; Viskontas, K.; Lengvinas, D.; Veitas, G.; Gadonas, D.; et al. SYLOS Lasers–the Frontier of Few-Cycle, Multi-TW, KHz Lasers for Ultrafast Applications at Extreme Light Infrastructure Attosecond Light Pulse Source. *J. Phys. Photonics* **2020**, *2*, 45003.
29. Arber, T.D.; Bennett, K.; Brady, C.S.; Lawrence-Douglas, A.; Ramsay, M.G.; Sircombe, N.J.; Gillies, P.; Evans, R.G.; Schmitz, H.; Bell, A.R.; et al. Contemporary Particle-in-Cell Approach to Laser-Plasma Modelling. *Plasma Phys. Control Fusion* **2015**, *57*, 113001. [CrossRef]
30. Briesmeister, J.F. (Ed.) *MCNP^{TM}—A General Monte Carlo N-Particle Transport Code*; Code Version 4C, also Univ. of California Tech. Report UC-700; Los Alamos National Laboratory: Los Alamos, NM, USA, 2000.
31. Pukhov, A.; Meyer-ter-Vehn, J. Laser Wake Field Acceleration: The Highly Non-Linear Broken-Wave Regime. *Appl. Phys. B* **2002**, *74*, 355–361. [CrossRef]
32. Pukhov, A.; Gordienko, S.; Kiselev, S.; Kostyukov, I. The Bubble Regime of Laser–Plasma Acceleration: Monoenergetic Electrons and the Scalability. *Plasma Phys Control Fusion* **2004**, *46*, B179. [CrossRef]
33. Lu, W.; Tzoufras, M.; Joshi, C.; Tsung, F.S.; Mori, W.B.; Vieira, J.; Fonseca, R.A.; Silva, L.O. Generating Multi-GeV Electron Bunches Using Single Stage Laser Wakefield Acceleration in a 3D Nonlinear Regime. *Phys. Rev. Spec. Top.-Accel. Beams* **2007**, *10*, 61301. [CrossRef]
34. Sprangle, P.; Ting, A.; Tang, C.M. Radiation Focusing and Guiding with Application to the Free Electron Laser. *Phys. Rev. Lett.* **1987**, *59*, 202. [CrossRef] [PubMed]
35. Götzfried, J.; Döpp, A.; Gilljohann, M.F.; Foerster, F.M.; Ding, H.; Schindler, S.; Schilling, G.; Buck, A.; Veisz, L.; Karsch, S. Physics of High-Charge Electron Beams in Laser-Plasma Wakefields. *Phys. Rev. X* **2020**, *10*, 41015. [CrossRef]
36. Meyers, R.A. *Encyclopedia of Physical Science and Technology*; Academic Press: Cambridge, MA, USA, 2002. Available online: http://113.161.190.196:8080/thuvienso/handle/123456789/668 (accessed on 11 February 2022).
37. Qi, W.; Zhang, X.; Zhang, B.; He, S.; Zhang, F.; Cui, B.; Yu, M.; Dai, Z.; Peng, X.; Gu, Y. Enhanced Photoneutron Production by Intense Picoseconds Laser Interacting with Gas-Solid Hybrid Targets. *Phys. Plasmas* **2019**, *26*, 43103.

38. Chao, Y.; Cao, L.; Zheng, C.; Liu, Z.; He, X. Enhanced Proton Acceleration from Laser Interaction with a Tailored Nanowire Target. *Appl. Sci.* **2022**, *12*, 1153. [CrossRef]
39. Pretzler, G.; Saemann, A.; Pukhov, A.; Rudolph, D.; Schätz, T.; Schramm, U.; Thirolf, P.; Habs, D.; Eidmann, K.; Tsakiris, G.D.; et al. Neutron Production by 200 MJ Ultrashort Laser Pulses. *Phys. Rev. E Stat. Phys. Plasmas Fluids Relat. Interdiscip. Top.* **1998**, *58*, 1165. [CrossRef]
40. Salvatores, M.; Palmiotti, G. Radioactive Waste Partitioning and Transmutation within Advanced Fuel Cycles: Achievements and Challenges. *Prog. Part. Nucl. Phys.* **2011**, *66*, 144–166. [CrossRef]
41. Kishon, I.; Kleinschmidt, A.; Schanz, V.A.; Tebartz, A.; Noam, O.; Fernandez, J.C.; Gautier, D.C.; Johnson, R.P.; Shimada, T.; Wurden, G.A.; et al. Laser Based Neutron Spectroscopy. *Nucl. Instrum. Methods Phys. Res. A* **2019**, *932*, 27–30.
42. Zimmer, M.; Scheuren, S.; Kleinschmidt, A.; Mitura, N.; Tebartz, A.; Schaumann, G.; Abel, T.; Ebert, T.; Hesse, M.; Zähter, Ş.; et al. Demonstration of Non-Destructive and Isotope-Sensitive Material Analysis Using a Short-Pulsed Laser-Driven Epi-Thermal Neutron Source. *Nat. Commun.* **2022**, *13*, 1173.
43. Shalloo, R.; Najmudin, Z.; Hafz, N.; Li, S.; Papp, D.; Kamperidis, C. E-SYLOS: A KHz Laser Wakefield Driven Beamline for Radiobiological and Imaging Applications at ELI-ALPS. Available online: https://agenda.infn.it/event/17304/contributions/99022/ (accessed on 10 May 2022).
44. IBA. Available online: https://www.iba-industrial.com/accelerators (accessed on 10 January 2022).